



Variations of the effective elastic thickness reveal tectonic fragmentation of the Antarctic lithosphere



Bo Chen ^a, Carina Haeger ^{b,c}, Mikhail K. Kaban ^{b,*}, Alexey G. Petrunin ^{b,d}

^a School of Geosciences and Info-Physics, Central South University, Changsha, China

^b Helmholtz-Centre Potsdam – GFZ German Research Centre for Geosciences, Potsdam, Germany

^c Faculty for Earth Sciences, Free University of Berlin, Germany

^d Faculty of Earth Sciences, Goethe University, Frankfurt am Main 60438, Germany

ARTICLE INFO

Article history:

Received 12 January 2017

Received in revised form 9 May 2017

Accepted 8 June 2017

Available online 11 June 2017

Keywords:

Antarctica

Effective elastic thickness

Lithosphere

Gamburtsev Subglacial Mountains

Fan wavelet method

ABSTRACT

To this day, little is known about thermal and rheological properties of the Antarctic lithosphere. We derive the effective elastic thickness T_e as a proxy for these parameters by using ice thickness, bedrock topography and a combination of new satellite and high resolution terrestrial gravity data. Cross-spectral analysis based on the fan wavelet technique was employed to calculate T_e variations by means of admittance and coherence techniques. Our results confirm a clear tectonic division of Antarctica with predominantly high values in East Antarctica (EANT) ($T_e \sim 60$ –80 km) and low values in West Antarctica (WANT) ($T_e \sim 5$ –20 km). For the Transantarctic Mountains separating these provinces, we found T_e to be around 10 km along the whole chain which is comparable to WANT. Apart from this general division, we found fragmentation of the lithosphere within these provinces. Especially EANT doesn't represent a single lithospheric block but shows strong variations of T_e . The highest values are found around the Aurora Subglacial Basin ($T_e \sim 90$ km) and in Dronning Maud Land ($T_e \sim 80$ km). The minimum value of T_e within EANT (~15 km) is found in the Lambert Graben. Such a low value can be associated with active rifting in the Permian-Triassic, strong localized erosion or possibly the effect of a Cenozoic mantle plume. According to the coherence calculations, the weak zone extends to the Gamburtsev Subglacial Mountains (GSM), showing a distinct decrease of T_e to 25–30 km. Thus, this weak channel divides the previously mentioned strong blocks. However, the admittance analysis gives relatively high values ($T_e \sim 70$ km) for the GSM. Based on the analysis of the wavelength-dependent admittance and coherence results and misfits for several principal locations, we give some preference to the coherence based values.

© 2017 Elsevier B.V. All rights reserved.

1. Introduction

Knowledge of the thermal state and mechanical properties of the lithosphere is important for many geophysical applications (Burov and Diament, 1995). The thermo-mechanical structure of the lithosphere controls to a large extent the initiation and evolution of tectonic deformation processes (e.g. Willett et al., 1985). These parameters are also required to model vertical motions at the Earth's surface, such as glacial isostatic adjustment (GIA), which are of prime importance in monitoring the mass balance of the Antarctic ice sheet (e.g. Ramillien et al., 2006). Furthermore, it has been recently demonstrated that the dynamical behaviour of the Greenland ice shield depends not only on the climate changes but is also controlled to a large extent by the heat flow from the Earth interior (Petrunin et al., 2013). Therefore, this effect can also be important for Antarctica. To this day, Antarctica remains one of the least studied and understood areas in the world. Due to its

remoteness and the thick ice sheet covering over 99% of its surface (Lythe et al., 2001), geophysical in-situ measurements are still sparse over large parts of the continent. Heat flow measurements, which are the only direct constraints on the thermal state of the lithosphere, are extremely sparse in Antarctica, especially in the areas covered by the ice shield (e.g. Fisher et al., 2015). The thermal structure of the lithosphere can also be evaluated based on seismic tomography models (Goes et al., 2000; Tesauro et al., 2015) and magnetic anomalies (Maule et al., 2005). However, such models provide very low resolution for the Antarctic upper mantle. Basically, they only show the difference between the relatively hot West Antarctica (WANT) and the cold East Antarctica (EANT) with very thick lithosphere (Schaeffer and Lebedev, 2013; Shapiro and Ritzwoller, 2004).

Only few studies were conducted to study the lithospheric structure in the internal areas of Antarctica. Seismic studies for example have been hindered by the sparsity of stations and very low intracontinental seismicity (Reading, 2007), yet improvements in surface wave studies provide S-velocity maps both on global (Schaeffer and Lebedev, 2013) and continental scales (An et al., 2015). The latter also present

* Corresponding author.

E-mail address: kaban@gfz-potsdam.de (M.K. Kaban).

information on Moho depth from their surface wave tomography as well as from a compilation of previous seismic studies. An Antarctic-wide collection of gravity data has been presented by Scheinert et al. (2016). All of these studies image very well the difference between the younger WANT and the older EANT, while smaller structures within the East Antarctic Craton remain unresolved.

Alternatively, there exists an integrative parameter, namely the effective elastic thickness of the lithosphere (T_e), which directly relates to the thermal state and rigidity of the lithosphere and can be used as their proxy. T_e is the thickness of an idealized elastic plate that would bend as the lithosphere under the same applied loads and can be used to quantify the lithospheric strength (Burov and Diamant, 1995). This parameter can be determined based on cross-spectral analysis of the gravity field and surface topography by applying various methods (Forsyth, 1985; Watts, 2001). Only a limited number of studies on T_e have been conducted in Antarctica, which still provide very inconsistent estimates of this parameter. Based on old and sparse data sets, Stern and ten Brink (1989) have already found indications for a transition from weak lithosphere in West Antarctica (WANT) to stronger lithosphere in East Antarctica (EANT) underneath the Transantarctic Mountains (TAM). ten Brink et al. (1997) analysed a 312-km-long traverse in the hinterland of the TAM and fitted the topography and gravity with an 85-km-thick elastic plate. Furthermore, Yamasaki et al. (2008) studied T_e by looking at the half-wavelength of the TAM and determined a very high value of this parameter (~100 km). Ferraccioli et al. (2011) calculated variations of T_e in the Gamburtsev province in East Antarctica and found that T_e varies from 30 km to >70 km in the central part. Recent satellite missions provide us with homogeneous gravity models on global scales (Förste et al., 2014), including areas where no other data are available. These data can be supplemented by detailed terrestrial and airborne gravity measurements, which have been strongly expanded during the last decade (Scheinert et al., 2016). Furthermore, Fretwell et al. (2013) collected data from various methods to compile improved grids of ice thickness, surface and bedrock elevation within Bedmap2, providing clearer images of the surface loading of the Antarctic continent. On the basis of these models, cross-spectral analysis of topography and gravity data can be used to determine T_e . McKenzie et al. (2015) have made estimates of T_e for Antarctica based on these data. However, they are limited to a comparison between East and West

Antarctica. Also, the obtained values (21 km and 5 km, correspondingly) are unusually low for continental areas.

In this study, we determine variations of the effective elastic thickness over the Antarctic continent by using modern methods based on a fan wavelet technique for the cross-spectral analysis of the gravity data and the topography adjusted for variations of the bedrock topography and ice thickness (Kirby and Swain, 2011, 2004). We determine both admittance and coherence of the Bouguer gravity anomalies and topography. A comparison of these results allows to resolve reliable features of the T_e pattern and compare them with the Antarctic tectonics and dynamic behaviour of the ice shield.

2. Tectonic setting of Antarctica

Antarctica is almost entirely covered by thick ice caps with a maximum thickness of nearly 4500 m (Fig. 1). Large parts of its bedrock topography lie below sea level (Fretwell et al., 2013). At large scales, it can be divided into two main tectonic provinces: The stable Precambrian shield of East Antarctica and West Antarctica, an amalgamation of thinner and hotter Cenozoic crustal micro-blocks (Dalziel and Elliot, 1982). EANT can be divided into several subglacial orogens and rifts. The largest structure is a subglacial plateau spanning 0°–100°E with its highest elevations in the Gamburtsev Subglacial Mountains and Dronning Maud Land (Fretwell et al., 2013). Enderby Land is characterized by only slightly less topography, yet previous studies of crustal thickness (e.g. O'Donnell and Nyblade, 2014) show it to reach similarly low values as the Basin structures of Wilkes and Aurora Subglacial Basins. The latter is a topographic depression lying up to 1 km below sea level, that may have been formed by erosion (Close et al., 2007). The Prince Charles Mountains are characterized by intraplate deformation and igneous intrusions caused by the collision of East and West Gondwanaland (565–500 Ma) (Veevers, 2007). The plateau is interrupted by a late Mesozoic transtensional basin that holds Antarctica's largest glacier, the Lambert Glacier (Reading, 2006).

WANT is a complex of several younger (mostly Jurassic and Cretaceous) microcontinental blocks that have moved independently from each other and from EANT until their amalgamation in the Cenozoic (Veevers, 2012). The most notable western Antarctic feature is the West Antarctic Rift System (WARS), a 750–1000 km wide crustal rift

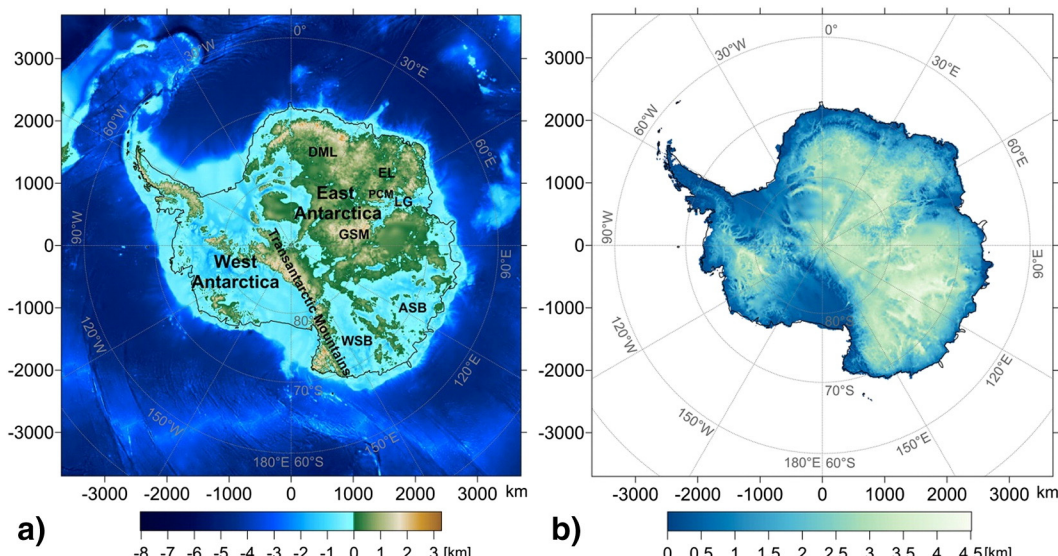


Fig. 1. (a) Bedrock topography of Antarctica (Fretwell et al., 2013) and bathymetry of the surrounding ocean (Schaffter et al., 2014). Key tectonic units: AP, Antarctic Peninsula; ASB, Aurora Subglacial Basin; DML, Dronning Maud Land; EL, Enderby Land; EWL, Ellsworth Land; FRIS, Filchner-Ronne Ice Shelf; GSM, Gamburtsev Subglacial Mountains; LG, Lambert Glacier; MBL, Marie Byrd Land; PCM, Prince Charles Mountains; RIS, Ross Ice Shelf; VH, Vostok Highlands; VL, Victoria Land; WARS, West Antarctic Rift System; WSB, Wilkes Subglacial Basin. (b) Ice thickness.

structure that mostly lies below sea level. Extension took place in two distinct phases: a prolonged period of broadly distributed extension in the Cretaceous and a phase of more focused extension in the Paleogene (Huerta and Harry, 2007). It is bordered by Mary Byrd Land, a region characterized by intraplate volcanism (Hole and LeMasurier, 1994).

EANT and WANT are separated by the Transantarctic Mountains (TAM), a 3500 km long and 200 km wide mountain chain with elevations of up to 4500 m (Morelli and Danesi, 2004). The TAM are the largest non-contractional mountains in the world (ten Brink et al., 1997) and their exact formation remains controversial. Three main uplift mechanisms have been suggested in the past: 1) Thermally driven uplift due to high temperatures at shallow depths (e.g. Smith and Drewry, 1984) possibly related to mantle plume activity (e.g. Behrendt, 1999); 2) Mechanically driven uplift caused by flexure and uplift of a broken plate edge (e.g. ten Brink and Stern, 1992); 3) The TAM were suggested to be the remaining margin of a Mesozoic West Antarctic plateau that collapsed (e.g. Huerta and Harry, 2007). Recently, van Wijk et al. (2008) proposed a new, rifting related model for the formation of the TAM. Since Antarctica occupied a central position in Gondwana prior to its breakup in the late Mesozoic, the Antarctic plate is bordered by eight different plates. The plate boundaries almost entirely consist of mid-ocean ridges (Torsvik et al., 2010) creating deviatoric stresses that eventually cause the onset of rifting near the border of East and West Antarctica. The West Antarctic Rift System develops in the weak crust of WANT while the stronger EANT craton remains unaffected. Rifting causes crustal material from the central rift zone to be transported toward its margins, its eastern margin being characterized by much higher (cratonic) strength. Hence, the crustal material accumulates at the boundary causing thickening and uplift of the crust. The van Wijk model also predicts the formation of a surface depression adjacent to the mountain chain that might correspond to the Wilkes Subglacial Basin. In this case, the Wilkes Subglacial Basin would be a flexural basin without crustal thinning.

3. Method

In order to estimate the effective elastic thickness, the lithosphere is commonly modelled as a thin elastic plate overlying a fluid substratum. It is bending under various types of loads, producing the gravity anomalies that we observe at the surface. The amount of the plate deflection primarily depends on an integrative parameter, namely the flexural rigidity D , which is related to the effective elastic thickness (T_e) as

$$D = ET_e^3 / [12(1-\sigma^2)], \quad (1)$$

where E is the Young's modulus (100 GPa) and σ is the Poisson's ratio (0.25). Analysis of the relationship and correlation (admittance or coherence, correspondingly) between the observed adjusted topography (topography, water, ice and, to some extent, density variations in the upper crust) and gravity anomalies in the spectral domain could provide potential information on the isostatic compensation of the lithosphere and give a measure of its mechanical properties (e.g. Audet and Mareschal, 2007; Watts, 2001).

The admittance method was first developed by Dorman and Lewis (1970), subsequently it was applied and improved in many studies (e.g. Banks et al., 1977; Forsyth, 1985; McKenzie and Bowin, 1976; Watts, 1978). A major development was contributed by Forsyth (1985), who combined the effects of surface and subsurface loading into the admittance method, and developed the coherence technique for T_e estimations. Currently, the admittance and coherence methods are widely used to estimate T_e of the lithosphere (e.g., Audet and Bürgmann, 2011; Chen et al., 2015a, 2015b; McKenzie et al., 2015; Pérez-Gussinyé and Watts, 2005; Watts, 2001). In this study, we apply both Bouguer admittance and coherence methods to estimate variations of T_e over Antarctica.

A number of different techniques have been used to calculate the spectrum of gravity and topography for admittance and coherence. The two extensively used ones are multitapers (McKenzie and Fairhead, 1997; Pérez-Gussinyé et al., 2004, 2009; Simons et al., 2000) and wavelets (Kirby and Swain, 2004, 2011; Stark et al., 2003). The multitaper technique was developed by Thompson (1982). It deals with spectral leakage well and has a good performance at short wavelengths, but its efficiency is restricted by the window size (Kirby, 2014). The wavelet technique was introduced in flexural studies by Stark et al. (2003) and Kirby and Swain (2004). Due to the wavelets' localization and variable spatial and wavenumber resolution, this method permits to locate T_e patterns with different wavelength, avoiding the restrictions due to the size of the computing window (Kirby, 2014). Furthermore, Kirby and Swain (2011) adjusted the central wavenumber of the Morlet wavelet to recover T_e variations with variable spatial resolution. The fan wavelet technique (Kirby and Swain, 2011, 2004) is applied to calculate the gravity and topography auto-spectra and the cross-spectrum in this study.

3.1. Calculation of admittance with the fan wavelet method

The admittance $Q(\mathbf{k})$ is the transfer function that relates the observed gravity anomaly and topography in the wavenumber domain (Dorman and Lewis, 1970),

$$B(\mathbf{k}) = Q(\mathbf{k})H(\mathbf{k}), \quad (2)$$

where $B(\mathbf{k})$ and $H(\mathbf{k})$ are the spectral representations of the Bouguer gravity anomalies and topography, \mathbf{k} is the two-dimensional wavenumber.

In practice, the calculated admittance is averaged in some wavelength interval to suppress the effect of noise. In the wavelet method, the admittance for Bouguer gravity anomaly and topography is defined as (Kirby and Swain, 2008):

$$Q_{obs}(s, x) = \frac{\text{Re}[\langle B_{sx\theta} H_{sx\theta}^* \rangle_\theta]}{\langle H_{sx\theta} H_{sx\theta}^* \rangle_\theta} \quad (3)$$

where B and H are the wavelet transforms of the Bouguer gravity and topography, respectively; $\text{Re}[\cdot]$ represents the real part. s and θ are the scale and azimuth of the Morlet wavelet, $*$ indicates complex conjugation; $\langle \cdot \rangle_\theta$ represents the averaging over azimuth. The wavelet admittance is a function of position x and wavelet scale s , which is related to an equivalent 1D Fourier wavenumber ($|\mathbf{k}|$) by the relation $|\mathbf{k}| = |\mathbf{k}_0|/s$, where $|\mathbf{k}_0|$ is the central wavenumber of the Morlet wavelet (Kirby and Swain, 2011).

This parameter $|\mathbf{k}_0|$ controls the spatial resolution of the T_e variations. The lowermost number provides better spatial resolution, but the result could be biased by noise. By increasing $|\mathbf{k}_0|$, we can suppress the effect of noise, however the resolution is decreasing. Therefore, it is necessary to choose a reasonable compromise. We use four values of the central wavenumber $|\mathbf{k}_0|$ given by Kirby and Swain (2011), 2.668, 3.081, 3.773 and 5.336, which correspond to the Morlet wavelets with the first sidelobes 1/16, 1/8, 1/4 and 1/2 of the central amplitude correspondingly. Since the wavelet transform is performed at a series of scales (s), the wavelength interval is determined by the choice of scales. Here we choose the scales spanning a dyadic grid from the Nyquist wavelength to the maximum dimension of the study area (Kirby, 2005; Kirby and Swain, 2011).

To model the admittance for specific values of T_e , a two-layer crustal model with both surface and subsurface loads is constructed under the assumption that the initial loading processes are statistically independent (Forsyth, 1985). Both the subsurface load and the compensation interface are assumed to be at the Moho depth (z_m), which corresponds to the Crust1.0 model (Laske and Masters, 2013). The combined-loading

predicted Bouguer admittance is given by Kirby, 2014:

$$Q_{pre}(s, x) = \frac{\mu_T k_T + \mu_B k_B f^2 r^2}{k_T^2 + k_B^2 f^2 r^2} \quad (4)$$

where f is the ratio of the internal load to the surface load, defined by (Forsyth, 1985; Kirby and Swain, 2011)

$$f^2(s, x) = \frac{\langle |W_i|^2 \rangle_\theta}{r^2 \langle |H_i|^2 \rangle_\theta} \quad (5)$$

$r = (\rho_c - \rho_f) / (\rho_m - \rho_c)$, ρ_c and ρ_m are the crustal (2800 kg/m^3) and mantle (3300 kg/m^3) densities, respectively; ρ_f is the density of the overlying fluid, $\rho_f = 0$ for the continent or $\rho_f = 1030 \text{ kg/m}^3$ for the ocean; μ_T , k_T , μ_B and k_B are the wavenumber-dependent coefficients that relate the initial surface and subsurface loads and the observed Bouguer gravity anomaly and topography (Kirby and Swain, 2011),

$$\begin{aligned} \begin{pmatrix} B \\ H \end{pmatrix} &= \begin{pmatrix} \mu_B & \mu_T \\ k_B & k_T \end{pmatrix} \begin{pmatrix} W_i \\ H_i \end{pmatrix} \\ k_B &= -(\rho_m - \rho_c)/\Phi \\ k_T &= 1 - (\rho_c - \rho_f)/\Phi \\ \mu_B &= 2\pi G (\rho_m - \rho_c) [1 - (\rho_m - \rho_c)/\Phi] e^{-|k|z_m} \\ \mu_T &= 2\pi G (\rho_m - \rho_c) [-(\rho_c - \rho_f)/\Phi] e^{-|k|z_m} \\ \Phi &= D|k|^4/g + \rho_m - \rho_f \end{aligned} \quad (6)$$

where W_i and H_i are the fan wavelet transforms of the initial surface and subsurface loads, respectively; g is the gravitational acceleration (9.8 m/s^2); G is the gravitational constant ($6.67 \times 10^{-11} \text{ m}^3 \text{ kg}^{-1} \text{ s}^{-2}$); z_m is the Moho depth.

3.2. Calculation of coherence with the fan wavelet method

The coherence is a measure of the phase relationship between the gravity anomalies and topography. Using the wavelet cross-spectrum of these fields and the auto-spectra of topography and gravity averaged over azimuth, the observed wavelet coherence is given by (Kirby and Swain, 2011, 2006)

$$\gamma_{obs}^2(s, x) = \frac{(\text{Re}[\langle B_{sx\theta} H_{sx\theta}^* \rangle_\theta])^2}{\langle B_{sx\theta} B_{sx\theta}^* \rangle_\theta \langle H_{sx\theta} H_{sx\theta}^* \rangle_\theta} \quad (7)$$

where we use the square of the real part of the coherency after Kirby and Swain (2009, 2011), and still name it “coherence” for simplicity. When the Bouguer gravity and topography are uncorrelated, the phases of the cross-spectra are randomly distributed and averaging cancels their coherence, whereas when the Bouguer gravity and topography are correlated, the averaging yields a high coherence (Audet and Mareschal, 2007; Kirby, 2014).

In the coherence and admittance methods, we assume that the gravity and topography are a result of flexural compensation of surface and subsurface loads. “Gravitational noise” may occur, which is that part of the observed gravity field not considered in the model (McKenzie, 2003; Kirby and Swain, 2009). For Antarctica, the “gravitational noise” may stem from the correlated internal loads without topographic expression (e.g., Kirby and Swain, 2009). In addition, the unrecovered surface topography after the removal of Quaternary ice loads (Pérez-Gussinyé et al., 2004) may also be a potential source of noise in the coherence and admittance analysis.

Reliability of the estimates with the coherence method can be evaluated by calculating the normalized squared imaginary part (NSIP) of

the free air coherency ($\bar{\Gamma}_{F,I}^2$) (Kirby and Swain, 2009):

$$\Gamma_F(s, x) = \frac{\langle G_{sx\theta} H_{sx\theta}^* \rangle_\theta}{\langle G_{sx\theta} G_{sx\theta}^* \rangle_\theta^{\frac{1}{2}} \langle H_{sx\theta} H_{sx\theta}^* \rangle_\theta^{\frac{1}{2}}}, \bar{\Gamma}_{F,I}^2 = \frac{(\text{Im}[\Gamma_F])^2}{|\Gamma_F|^2} \quad (8)$$

where $G_{sx\theta}$ is the wavelet transform of the free air gravity anomalies; $\text{Im}[\cdot]$ represents the imaginary part. As suggested by Kirby and Swain (2009), the coherence (and consequently T_e) may be biased by “gravitational noise”, when the maximum value $\bar{\Gamma}_{F,I}^2$ around the Bouguer transition wavelength exceeds 0.5. The Bouguer transition wavelength corresponds to an often-sharp rollover from 1 to 0 in a coherence curve, and is strongly dependent on the magnitude of T_e (Kirby, 2014).

Similar to the admittance method, the same two-layer crustal model with both surface and subsurface loads is employed to model the predicted coherence. Using the assumption of uncorrelated loading (Forsyth, 1985), the predicted coherence can be determined as (Kirby and Swain, 2011):

$$\gamma_{pre}^2(s, x) = \frac{(\mu_T k_T + \mu_B k_B f^2 r^2)^2}{(\mu_T^2 + \mu_B^2 f^2 r^2)(k_T^2 + k_B^2 f^2 r^2)} \quad (9)$$

The observed admittance or coherence is compared with the model predictions for a range of T_e values. T_e is obtained by minimizing the root-mean-square difference between the observations and model predictions at each grid node of the study area. In order to suppress the increased effect of noise at short wavelengths, the misfit (ϵ) is weighted by the inverse of the equivalent Fourier wavenumber (Kirby and Swain, 2006, 2008), and is calculated through

$$\epsilon = \sqrt{\frac{\sum_{i=1}^N [\gamma_{obs}^2(|k|_i) - \gamma_{pre}^2(|k|_i)]^2 / |k|_i^2}{\sum_{i=1}^N 1 / |k|_i^2}} \quad (10)$$

where N is the number of the equivalent wavenumber.

4. Initial data

The free air gravity disturbances were obtained combining the models Eigen-6c4 (Förste et al., 2014) and AntGG (Scheinert et al., 2016). The Eigen-6c4 dataset combines terrestrial and satellite (GRACE, GOCE and LAGOS) data to a global grid with a resolution of up to 2190 spherical harmonics degree/order. However, actual horizontal resolution of this data set depends on the used terrestrial data, which for Antarctica doesn't exceed 200 km, therefore limiting it to the satellite only solution. AntGG is a compilation of ground-based, airborne and shipborne gravity anomaly measurements over Antarctica providing short wavelength gravity information not present in the satellite data. It consists of 13 million data points covering ~73% of the continent at 10 km resolution. However, this data set contains many gaps causing its long-wavelength part to be biased. Therefore, we combine it with the satellite based gravity maps. Above the wavelength 250 km, chiefly the satellite model is used, below 150 km, the data from AntGG are employed with gradual transition within this wavelength interval.

In order to obtain the Bouguer gravity anomalies (Fig. 2a), we remove the gravity effect of the topography, ice and water columns from the free air gravity disturbances. Information on surface elevation, bed elevation and ice thickness up to 60°S was provided by Bedmap2 (Fretwell et al., 2013), bathymetry north of 60°S is taken from the global bathymetry grids from RTopo-2 (Schäffer et al., 2014). The gravity effect is calculated within a 222.4 km (2°) radius around each point. All spherical effects are taken into account in the calculations (Kaban et al., 2016). The reference density of the upper crust is $\rho_t = 2670 \text{ kg/m}^3$ and the density of water is $\rho_w = 1030 \text{ kg/m}^3$. Since the density of ice is

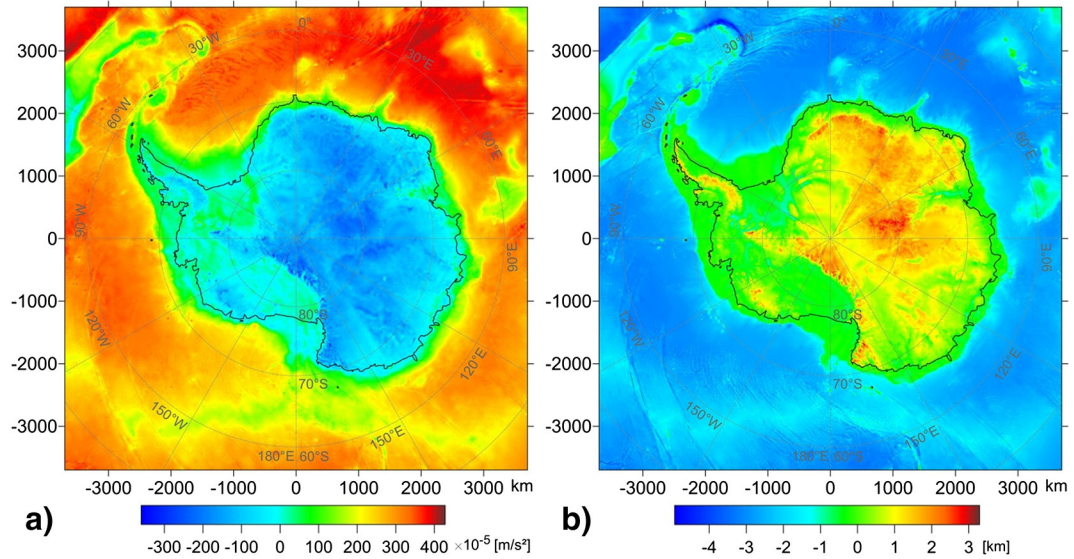


Fig. 2. (a) Bouguer gravity anomalies. (b) Adjusted topography combining variations of the bedrock elevation, ice and water.

temperature-pressure dependent, and ice temperatures vary strongly with depth within the ice shield, we tested the influence of these variations on the gravity effect. Within reasonable temperature variations in Antarctic glacial settings of approximately -10 to -50 °C (Price et al., 2002), we found the gravity variation to be negligible ($\pm 0.35 \times 10^{-5}$ m/s²) thus assuming from here on out the constant average ice density $\rho_i = 920$ kg/m³. Based on these values, we have also calculated the adjusted topography (H) by compressing the ice and water columns to the standard density of the crust:

$$H = h_b + \frac{\rho_w}{\rho_t} h_w + \frac{\rho_i}{\rho_t} h_i \quad (11)$$

where h_b is the bedrock topography, h_w and h_i are the heights of the water and ice, respectively.

All data grids were produced using Polar Stereographic Projection (Snyder, 1987) based on the WGS84 ellipsoid with true scale at 71°S with a grid size of 10 by 10 km. The calculated adjusted topography is shown in Fig. 2b.

5. Results

Variations of T_e of the Antarctic lithosphere were estimated using the fan wavelet method to determine the admittance and coherence of the Bouguer gravity anomalies and adjusted topography. As described above, we have used four values of the central wavenumber $|k_0|$, 2.668, 3.081, 3.773 and 5.336.

5.1. Spatial variations of T_e by coherence inversion

Variations of the effective elastic thickness computed with the coherence method for different values of the central wavenumber of the Morlet wavelet $|k_0|$ are shown in Fig. 3. All figures are consistent. One of the dominant features is the division of Antarctica along TAM. West Antarctica including TAM is chiefly characterized by a very weak lithosphere, while to the east, high values of T_e are prevalent excluding the area around the Lambert Graben (LG). Later on, we discuss specific patterns of these variations. The maximum spatial resolution of the obtained map corresponds to the minimum central wavenumber of the Morlet wavelet $|k_0| = 2.668$. However, the patterns of this map are unstable, so a lot of the small anomalies likely represent artefacts because the lower $|k_0|$ wavelets indicate greater uncertainty on the T_e estimation (Kirby and Swain, 2011). This is also confirmed by a relatively wide area,

where the parameter $\bar{\Gamma}_{F,I}^2 > 0.5$ and the results are unreliable (Fig. 3a). In contrast, the maximum $|k_0| = 5.336$ provides a stable and smooth map, but amplitudes of the main anomalies are damped and some of them disappear (Fig. 3d). The two intermediate values give a reasonable compromise (Fig. 3b–c). Possible uncertainty of the T_e estimations is assessed based on the misfit curve. Following Watts et al. (2006) we determine lower and upper limits of T_e for the misfit, which exceeds the minimum by 5% ($\varepsilon = 1.05\varepsilon_{\min}$). The upper and lower values for $|k_0| = 3.773$ are shown in Fig. 5.

In order to discuss reliability of the results, we analyse the coherence and other parameters calculated in eight points (Fig. 3c) for several key features of Antarctica. The graphs showing the observed and predicted coherence with other parameters of the calculations are shown in Fig. 5. The maximum $T_e = 92$ km is found for ASB. This value corresponds to a drop of the coherence at the wavelength 800–900 km. The misfit demonstrates a pronounced minimum, which supports that the result is reliable. Below 200 km, the parameter NSIP quickly increases with decreasing wavelength. Therefore, the quality of the initial data is limited to this wavelength (ca. 100 km in the spatial domain). Similar results are obtained for DML, which represents another area with high $T_e = 79$ km. In contrast, for GSM in the center of Antarctica we obtain a relative low $T_e = 26$ km. Moreover, this is likely the maximum value corresponding to the first decrease of the observed coherence, since the misfit is weighted by the inverse of the equivalent Fourier wave number. This is clearly demonstrated by the misfit curve, which is almost flat below 26 km up to zero. This proves that the lithosphere is relatively weak in the area of GSM compared to DML and ASB. The weakest lithosphere in East Antarctica is found in the area of LG ($T_e = 15$ km). This value is very well determined, in particularly due to the high quality data, which is demonstrated by near zero NSIP until the wavelength ~50 km.

One of the new findings is the low value of T_e (9–11 km), which is determined for TAM. The quality of the data is not as good as in the previous cases, but the range of acceptable T_e values (approximately from 0 to 25 km) indicates that this structure is really characterized by a relatively weak lithosphere. Consequently, also the fits between observed and predicted coherence values are not as clear as in other locations, since the fitted decrease is slightly steeper than the overall decrease for both examples. Yet, the fitted curve still remains within the observation uncertainties in almost all points. These results are consistent for the whole TAM chain. Therefore, TAM can be linked to the weak lithosphere of West Antarctica. The last one is chiefly

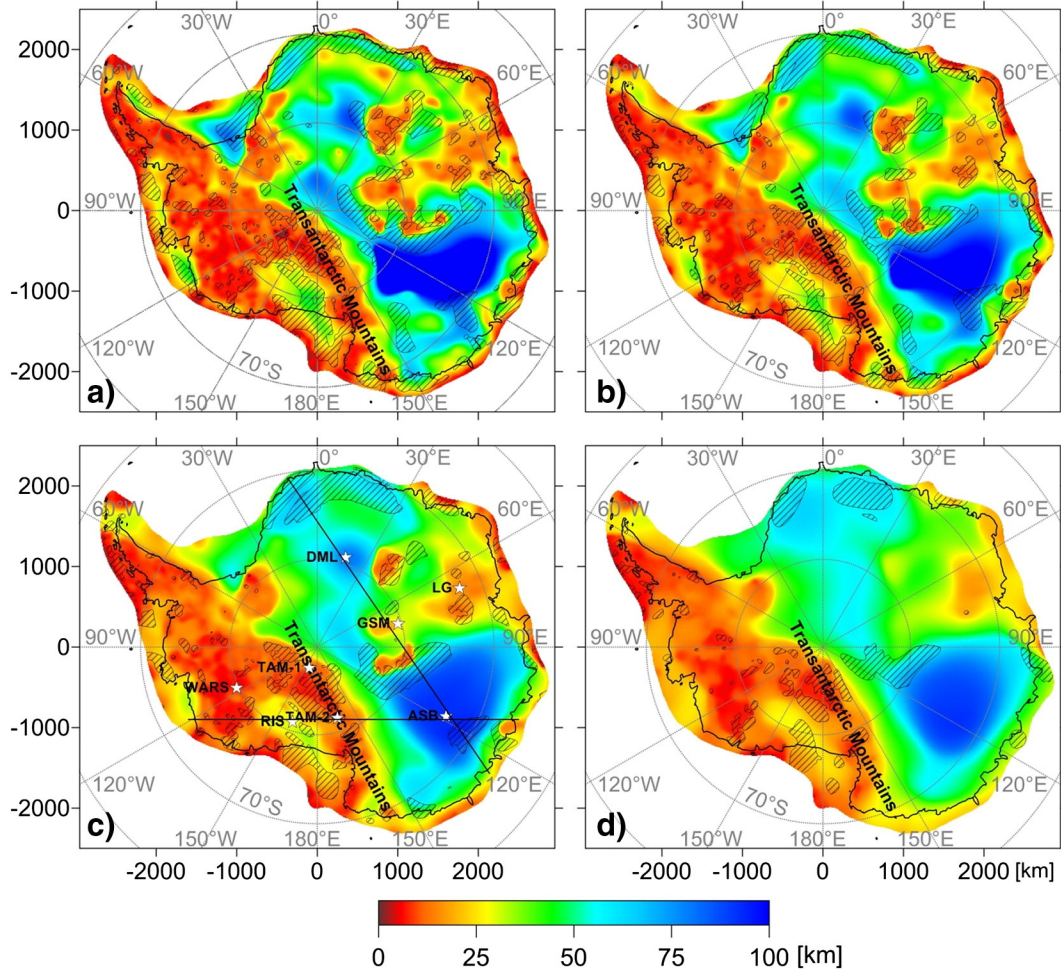


Fig. 3. Variations of T_e obtained with the coherence method. Four different values of the central wavenumber of the Morlet wavelet $|k_0|$ are considered: (a) 2.668, (b) 3.081, (c) 3.773 and (d) 5.336. The hatched patterns show the areas, where the maximum value of the normalized squared imaginary part of the free air coherency (Eq. 7) is larger than 0.5 and the results might be biased. The white stars show locations, for which the calculation results are demonstrated. Abbreviations as in Fig. 1.

characterized by $T_e < 15$ km, as demonstrated for the West Antarctic rift system ($T_e = 6$ km, Fig. 5). The only exclusion is the area of the Ross Ice Shelf (RIS), for which relatively high values of $T_e = 20$ –

40 km are obtained. As it is visible from Fig. 5-RIS, the abrupt decrease of the coherence at the wavelength ~ 300 km indicates that this result is trustworthy.

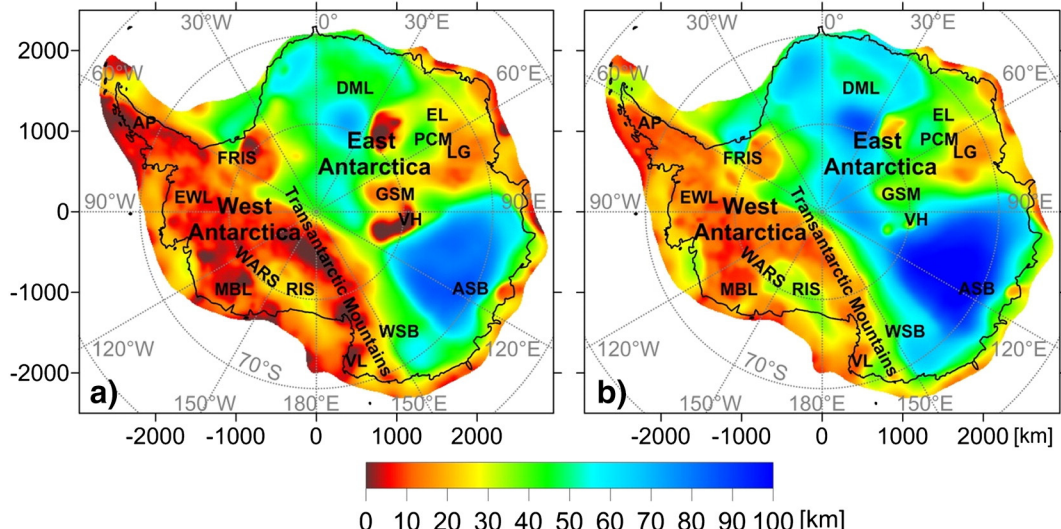


Fig. 4. Lower (a) and upper (b) boundaries of the T_e estimation with the coherence method for $|k_0| = 3.773$. These values correspond to the misfit $\varepsilon = 1.05 \varepsilon_{\min}$ (Watts et al., 2006). Abbreviations as in Fig. 1.

5.2. Spatial variations of T_e by admittance inversion

Variations of T_e computed with the admittance method are shown in Fig. 6. In general, they are consistent with the coherence results. We also observe a clear difference between the western and eastern parts of Antarctica and TAM are also linked to the weak lithosphere of WANT. However, there exist several principal differences, for example, GSM are characterized by high values of T_e similar to DML and ASB. The upper and lower values of T_e , which are determined based on the misfit curves for $|\mathbf{k}_0| = 3.773$, are shown in Fig. 7.

We analyse the calculated admittance for the same eight locations as for the coherence results. The observed and predicted admittance with the misfit for eight selected points (Fig. 6c) is shown in Fig. 8. It is clear from these graphs as well as from the comparison of the lower and upper limits of T_e (Figs. 4 and 7) that the admittance determinations of T_e are more uncertain than corresponding estimates with the coherence method. Comparison of Figs. 5 and 8 reveals that the Bouguer coherence inversion provides a better fit between the observations and predictions. In fact, a good fit of the observed and predicted admittance is obtained for two locations

only (TAM-2 and WARS). As pointed out by Forsyth (1985) and Kirby and Swain (2008), the admittance estimates of T_e are highly sensitive to the internal load (unknown crust and mantle density anomalies) compared to the coherence estimations; and the first ones frequently overestimate T_e .

However, in most cases the admittance results agree with the T_e estimations obtained with the coherence method. Both ASB and DML regions are characterized by very high T_e evidencing for a very strong lithosphere. In contrast, T_e values for WARS are generally very low. For the TAM we obtain different values for two locations (23 km and 10 km). However, in both cases, the misfit between the observed and predicted values has no clear minimum. Therefore, any value within the interval from 0 km to 35 km would almost equally fit the observations. The high T_e for GSM is based on the very long wavelengths (>1000 km) and doesn't fit the observed values at the mid and short wavelengths. The long wavelength signal in this area is likely biased by extraneous factors, which is visible in the normalized squared imaginary part (NSIP) of the free air coherency (Fig. 5). For LG, the obtained value ($T_e = 40$ km) is relatively high. However, the misfit curve is nearly flat from 0 km to approximately 60 km implying that T_e may be equal to any value within this interval.

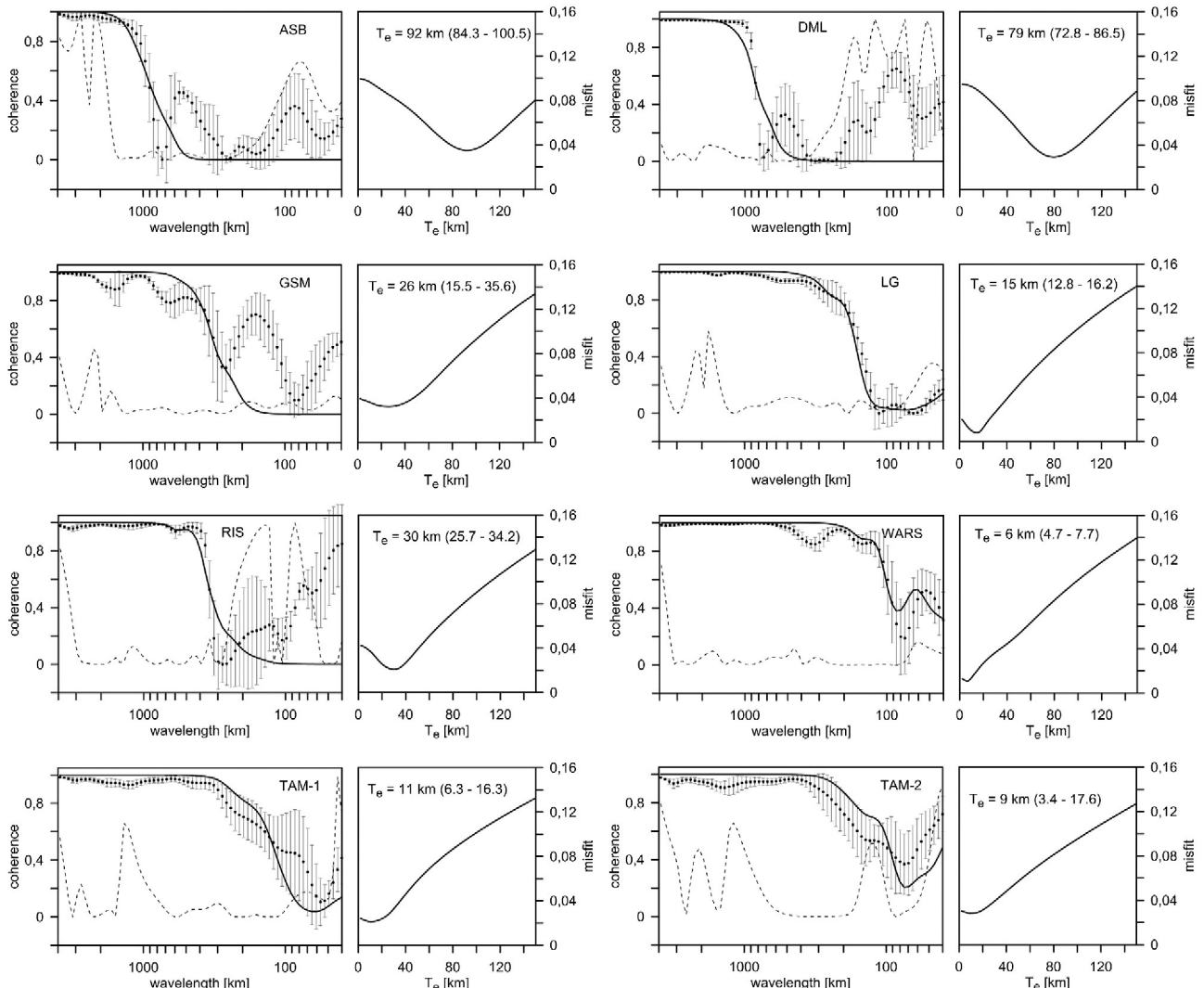


Fig. 5. Coherence and misfit for eight locations in Antarctica (Fig. 3c) for $|\mathbf{k}_0| = 3.773$. Left graphs show coherence depending on the wavelength. Points with uncertainties represent observations, solid line – predicted (model) values, and dashed line – the parameter NSIP (Eq. 8). Right graphs show misfit depending on T_e . The lower and upper boundaries corresponding to the misfit $\varepsilon = 1.05 \varepsilon_{\min}$ are shown in parentheses. Abbreviations as in Fig. 1.

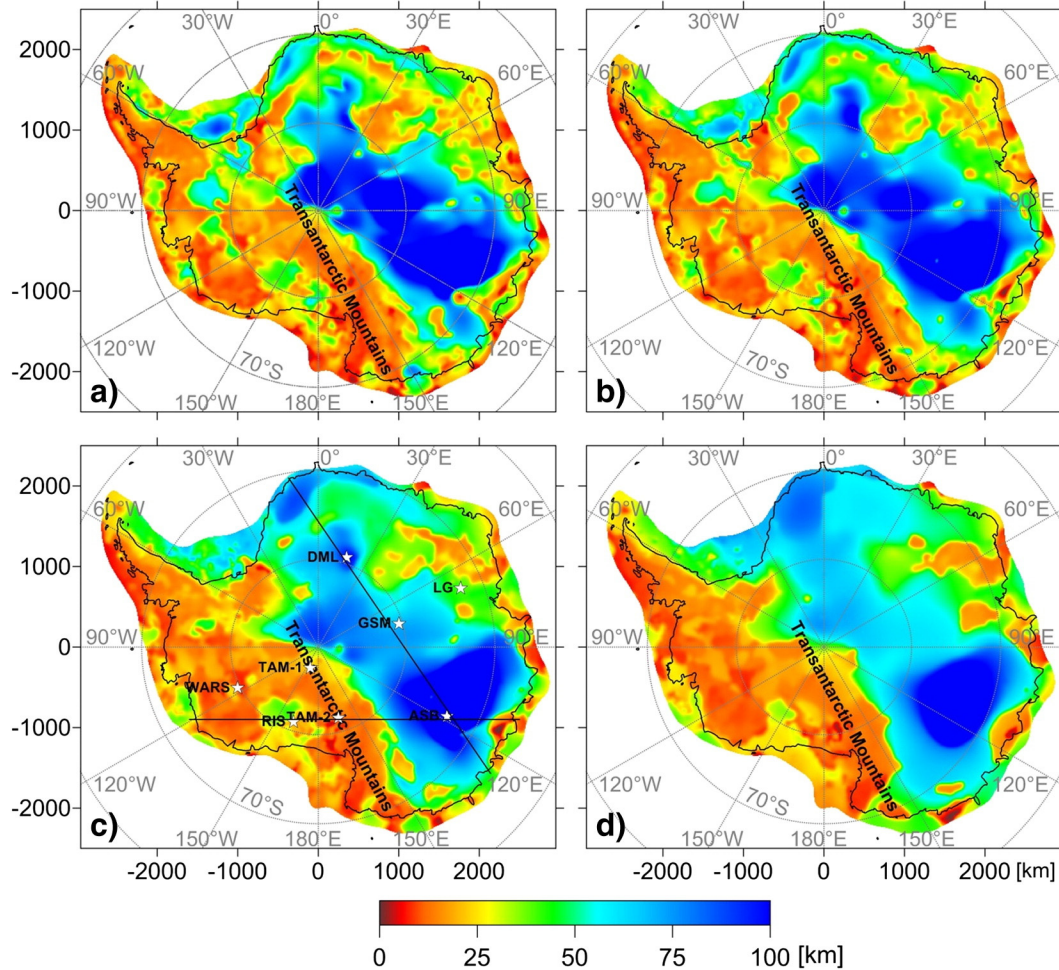


Fig. 6. Variations of T_e obtained with the admittance method. Four different values of the central wavenumber of the Morlet wavelet $|k_0|$ are considered: (a) 2.668, (b) 3.081, (c) 3.773 and (d) 5.336. The white stars show locations, for which the calculation results are demonstrated. Abbreviations as in Fig. 1.

6. Discussion

In the discussion we chiefly refer to the results obtained with the coherence method since they better fit to the observed values and are less uncertain.

Analysis of the variations of the effective elastic thickness within the Antarctic continent reveals a clear distinction between strong lithosphere in the east and weak lithosphere in the west, correlating well with the position of the East Antarctic Craton and the thinner, hotter West Antarctic terrains. Major geological features of East Antarctica

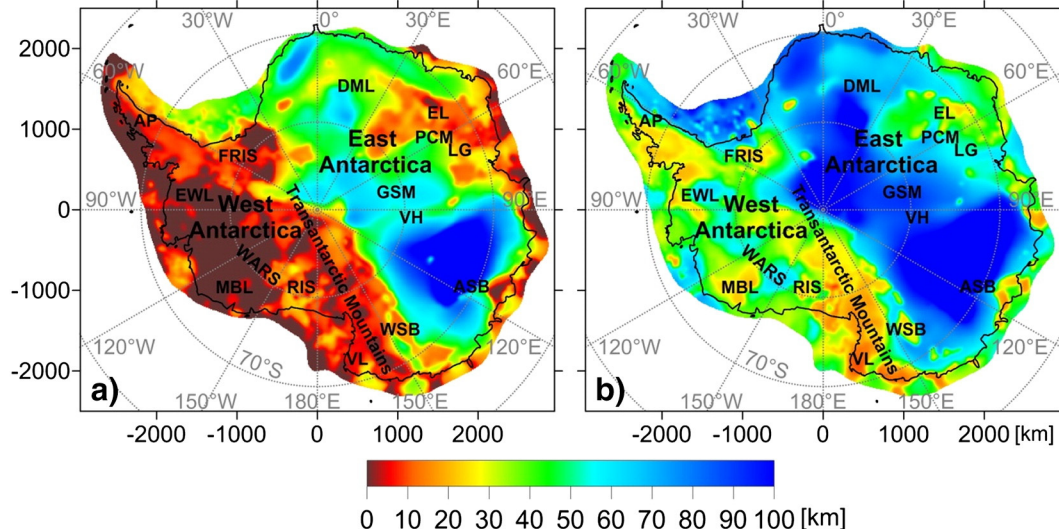


Fig. 7. Lower (a) and upper (b) boundaries of the T_e estimation with the admittance method for $|k_0| = 3.773$. These values correspond to the misfit $\varepsilon = 1.05 \varepsilon_{\min}$ (Watts et al., 2006). Abbreviations as in Fig. 1.

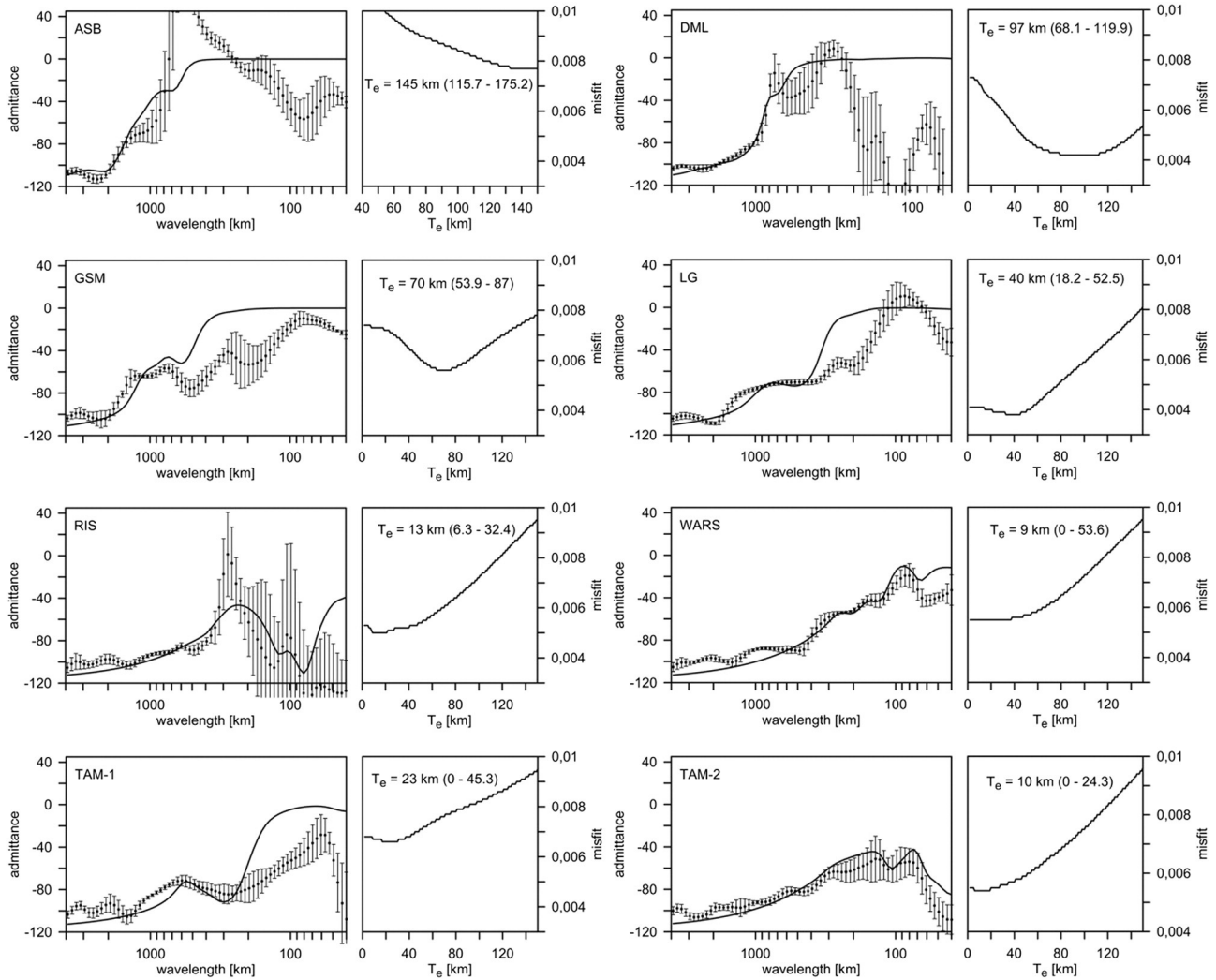


Fig. 8. Admittance and misfit for eight locations in Antarctica (Fig. 5c) for $|k_0| = 3.773$. Left graphs show admittance depending on the wavelength. Points with uncertainties represent observations, solid line – predicted (model) values. Right graphs show misfit depending on T_e . The lower and upper boundaries corresponding to the misfit $\varepsilon = 1.05 \varepsilon_{\min}$ are shown in parentheses. Abbreviations as in Fig. 1.

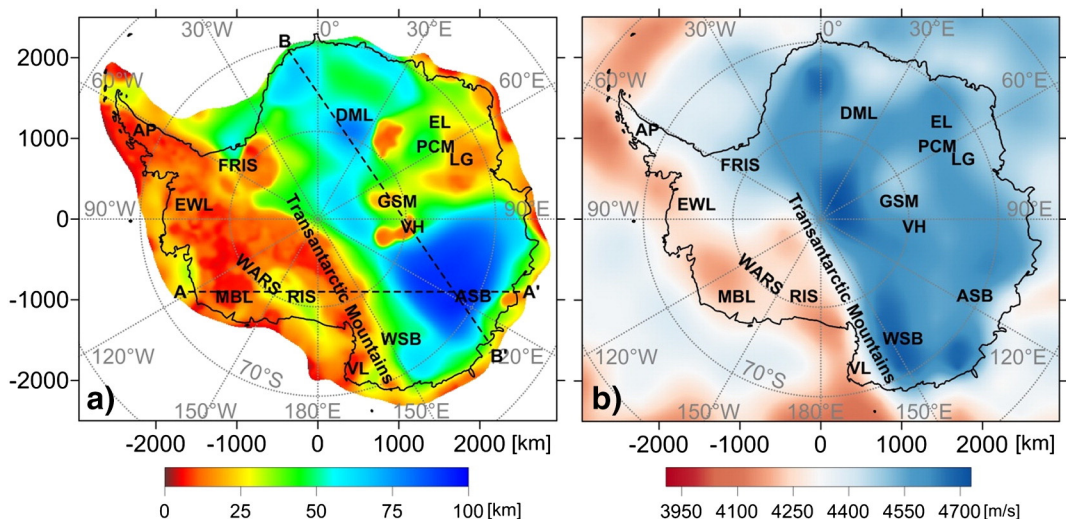


Fig. 9. (a) Variations of T_e obtained by the coherence method for a central wavenumber of the Morlet wavelet $|k_0| = 3.773$. Dashed lines represent the locations of the profiles shown in Fig. 8. (b) Tomography model SL2013-2.1 (Schaeffer and Lebedev, 2013) of S-velocities at a depth of 100 km. Abbreviations as in Fig. 1.

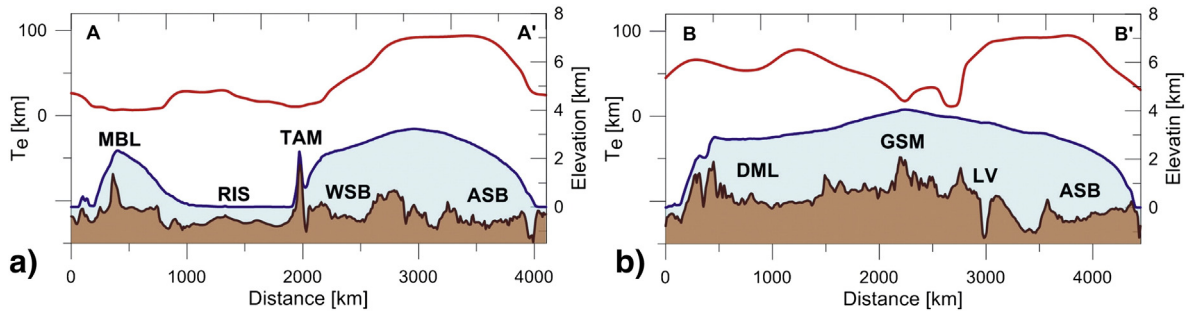


Fig. 10. Profiles across Antarctica showing the Effective Elastic Thickness T_e determined by the coherence analysis (upper curve), surface elevation (blue) and bedrock elevation (brown). Locations are shown in Fig. 7. Abbreviations as in Fig. 1.

formed in the Precambrian with a tectonic reactivation during the Paleozoic and early Mesozoic (Boger, 2011). Consequently, it is chiefly characterized by thick cold lithosphere with relatively high values of T_e and presumably low heat flow values (e.g. Shapiro and Ritzwoller, 2004). In contrast, West Antarctica is dominated by relatively young terrains formed and developed in the Mesozoic and Early-Mid Cenozoic. The large scale features in our T_e map generally correlate well with seismic tomography studies, which imaged low S-velocities in WANT and high velocities in EANT at a depth of 100 km according to the model SL2013-2.1 (Schaeffer and Lebedev, 2013) (Fig. 9b). Apart from the general distinction, the SL2013-2.1 model only shows little structure and we should take care not to over interpret these small scale features. A study of McKenzie et al. (2015) examining average T_e for EANT and WANT using admittance calculations also gives a clear distinction between these provinces. Yet their values (21 km and 5 km respectively) are substantially lower than our findings. There might be several reasons for these discrepancies. First, we use the gravity model, which includes high resolution terrestrial observations. Second, in our method, the load ratio is wavenumber-dependent, which is determined by the load deconvolution process (Lowry and Smith, 1994) from the observed gravity and topography data. In contrast, McKenzie et al. (2015) used an analytical formula for the model admittance with a uniform load ratio to fit the observed admittance. Third, the misfit curve for EANT calculated by McKenzie et al. (2015) has no clear minimum and any value of T_e exceeding ~17 km would provide an almost equal fit to the observed admittance. Therefore, the observed value of 21 km does not represent an exact estimate, but a lower bound for T_e . On the other hand, our results based on the coherence analysis well correspond globally to the T_e estimates for similar tectonic provinces (e.g. Audet and Bürgmann, 2011; Tesauro et al., 2012).

As previously mentioned, EANT and WANT are separated by the Transantarctic Mountains. In a previous study, ten Brink et al. (1997) derived an effective elastic thickness of 70 km for the TAM based on the analysis of a very limited area, thus attributing the mountain side to Eastern Antarctica with its thick and strong lithosphere. Our results reveal a very weak lithosphere with T_e about 10 km, which characterizes the whole mountain chain. This suggests that the TAM are located on the western side of the margin between EANT and WANT, supporting the theory of van Wijk et al. (2008) that formation and further uplift of the TAM is connected to the tectonic history of the West Antarctic rift system (WARS) starting at the Late Cretaceous with an active uplift phase at the Mid-Late Cenozoic. At the first stage (about 100 Ma) the entire area of the WARS was subjected to uniform extension. During the second stage in the Late Paleogene, the distributed extension has localized within a narrow zone close to the TAM (Huerta and Harry, 2007) that was accompanied by volcanic activity and initiation of the main stage of the TAM uplift. Our results support this scenario in general (Figs. 9 and 10), however one should note, that the T_e map reflects only present-day thermo-mechanical state of the lithosphere and can provide an additional knowledge on tectonic history only indirectly. The Wilkes Subglacial Basin (WSB) in the hinterland of the TAM

exhibits a transition between WANT and EANT with a gradual increase of T_e (Fig. 10a).

According to our results, East Antarctica (EANT) doesn't represent a homogeneous lithospheric block, but is clearly divided into several parts (Fig. 9a) and thus offers insight into the lithospheric structure of EANT that has not been imaged in the past, e.g. by seismic tomography (compare Fig. 9). The strongest lithosphere with T_e up to 90 km is found between 90°E and 130°E around the Aurora Subglacial Basin (ASB) (Fig. 9). Tectonic and geological reconstructions suggest that the ASB basement consists of Mesoproterozoic to Archean rocks of the Mawson and Crohn Craton that sutured in the late Mesoproterozoic and remained comparably unaffected by tectonic processes since then (Boger, 2011). Several studies identified Terre Adélie Land just east of the ASB as the nucleus of Antarctica (e.g. Fanning et al., 1988; Flöttmann and Oliver, 1994). Hence, the ASB and surrounding are formed of very old, cold and dense lithosphere explaining the sub-sea-level topography, fast seismic velocities and high lithospheric strength (Fig. 9). Another block characterized by high T_e , which is only slightly lower than in the ASB, is represented by the Central Dronning Maud Land (DML) (Figs. 9–10). According to Boger (2011), this is also an Archean fragment of the Kaapvaal Craton of southern Africa that collided with central Antarctica in the Cambrian.

The strong nuclei associated with the DML and ASB are divided by a zone of relatively low T_e as demonstrated by the results based on the coherence analysis (Figs. 3, 9 and 10). The minimum T_e within EANT (~15 km) is found in the area of the Lambert Graben (LG). LG is described as a failed rift system that formed during the Carboniferous to Cretaceous (Harrowfield et al., 2005; Lisker et al., 2003; Powell et al., 1988) that holds the Lambert Glacier (Reading, 2006). The presence of the glacier also caused strong localized erosion (>2 km) since the Oligocene (Thomson et al., 2013). The low values of T_e might be also explained by possible passing of a Cenozoic mantle plume below the LG and GSM (Sleep, 2006) causing the LG valley incision. Both explanations would be consistent with our observations, yet a distinction between them cannot be given by our results at this time, but would require further study. The anomalously low values of T_e in the LG correlate well with high ice velocities within the area (Rignot et al., 2011) that might assume interconnection between the T_e , heat flow, and ice dynamics. The results obtained for the Gamburtsev Subglacial Mountains (GSM) are controversial. According to the coherence analysis, T_e is reduced to 25–30 km compared to the DML and ASB (Fig. 9). As already mentioned, this result seems to be reliable because the normalized squared imaginary part (NSIP) of the free air coherency is close to zero in the whole wavelength interval used for determination of T_e for GSM with the coherence method ($\lambda < 1500$ km, Fig. 5). Consequently, the Free-air coherency in the GSM is among the highest observed in the continent because the ice shield prevented significant erosion during the last 30 Ma, as already reported by Paxman et al. (2016). Furthermore, the decrease in coherence fitted for $T_e = 26$ km (Fig. 5) is the drop with the maximum wavelength, therefore, this is the highest possible value of T_e . This result is close to the result of Paxman et al. (2016), who calculated free air

admittance and Bouguer coherence suggesting very low T_e of 0–1 km and 5–14 km, respectively. We also observe a relative minimum of V_s in this area at a depth of 100 km as demonstrated by the model of Schaeffer and Lebedev (2013) (Fig. 9b), hinting at possibly anomalous lithosphere in the larger GSM area. Sleep (2006) suggested a presence of a plume head beneath the GSM and Vostok highlands, which reheated and weakened the lithosphere in this region and caused an uplift of the GSM explaining our observations of reduced T_e . Recently, a bifurcation of the rift bounding the GSM that would weaken the lithosphere and thus lower T_e , was also suggested by Phillips and Lüfer (2009).

On the other hand, the admittance analysis gives relatively high values of T_e (~70 km) for the GSM, although the model admittance fits the observations at the long wavelengths only ($\lambda > 700$ km, Fig. 8). This agrees with the result of Ferraccioli et al. (2011), who obtained approximately the same value based on the shape of the Moho, which is determined from the gravity data. It should be noted that this result, as well as our admittance analysis, could be seriously biased by the density heterogeneity of the crust and upper mantle, which is not taken into account in both studies. Actually, for measuring of elastic deformations one should determine horizontal gradients of the Moho, which are not well-constrained, even by seismic studies. Yet, we cannot completely reject the admittance model, although we give some preference to the result based on the coherence analysis determining reduced T_e for the GSM. To further clarify the thermo-mechanical state of the GSM lithosphere, a closer study of the region possibly with other, independent methods is necessary.

7. Conclusions

We used bedrock topography, ice thickness and a combination of new satellite and high resolution terrestrial gravity data to determine variations of the effective elastic thickness over the Antarctic continent. Both admittance and coherence were derived using modern cross-spectral analysis methods based on the fan wavelet technique. Analysis of the wavelength-dependent admittance and coherence results and other parameters for several principal locations has shown that the coherence based values are more reliable for the problem at hand and thus form the basis for interpretations in this study.

Generally, Antarctica's division into two distinct tectonic provinces is also seen in the lithospheric rigidity. While T_e is mostly high in the cratonic area of East Antarctica, West Antarctica is characterized by much lower values. The Transantarctic Mountains separate these domains, but if they form part of EANT or WANT remains somewhat enigmatic. We determined low T_e with values around 10 km for the entire mountain chain similar to what can be found in the entire western Antarctic domain. We thus suggest that the TAM are part of WANT.

Apart from the general distinction between EANT and WANT, we were also able to resolve smaller scale fragmentation within these blocks. Especially East Antarctica is not homogeneous in lithospheric strength as previously thought, but shows strong variations of T_e for different provinces. The highest effective elastic thickness can be found in the Aurora Subglacial Basin with surroundings ($T_e \sim 90$ km). Slightly lower values of $T_e \sim 70$ –80 km can be found in Dronning Maud Land. We interpreted this as a sign for very old, cold and strong lithosphere, which is also supported by tectonic and geological reconstructions (Boger, 2011). The weakest lithosphere ($T_e \sim 15$ km) within EANT appears in the Lambert Graben (LG). Such an anomalously low value, compared to the mean for EANT, might be explained by a combination of several factors such as primary tectonic weakness inherited from the Permian-Triassic active rifting phase of the LG (Harrowfield et al., 2005), strong localized erosion (≥ 2 km) along the LG since the Oligocene (Thomson et al., 2013), and possible influence of a Cenozoic mantle plume (Sleep, 2006).

According to the coherence based results, the weak zone extends from the LG toward the Gamburtsev Subglacial Mountains. The effective

elastic thickness of the GSM has been the subject of discussion (e.g. Ferraccioli et al., 2011; Paxman et al., 2016). The results based on the coherence analysis indicate that the effective elastic thickness is reduced to $T_e \sim 26$ km and support the assumption of low lithospheric strength within the GSM area. Anticipated heating by a mantle plume might be the cause of the lithospheric weakening (Sleep, 2006). On the other hand, the admittance results for the GSM give $T_e \sim 70$ km, which is not remarkably different from the ASB and DML. We suppose that the admittance results might be substantially biased by density variations within the lithosphere and therefore give some preference to the coherence analysis, which evidences for the reduced effective elastic thickness of the lithosphere.

The West Antarctic lithosphere is characterized generally by very low values of T_e (5–20 km), which agrees with the tectonic history of WANT. Since the Late Cretaceous the entire area of WANT has been affected by complex tectonic processes associated with late fragmentation of Gondwana, the WARS formation and accompanying magmatism. Local variations of T_e (e.g. such as a relative maximum in the Ross Ice Shelf) likely correspond to ancient and more strong terrains initially forming WANT (e.g. Mukasa and Dalziel, 2000).

Therefore, our T_e models present new insight into the lithospheric structure of Antarctica, because it shows lateral heterogeneity of the lithosphere that has not been provided previously by other (chiefly seismic tomography) methods. Instead of a comparably uniform strong cratonic lithosphere in EANT, our study reveals lithospheric fragmentation with both methods employed here. However, the exact extend and origin of this low T_e region within EANT remain somewhat unclear and would require further studying based on independent geophysical methods like for example thermo-mechanical modelling of the lithosphere.

Acknowledgements

We acknowledge funding from DFG (German Research Foundation), SPP-1788 (Grant KA2669/4-1), Grant PE2167/1-1, National Natural Science Foundation of China (Grant no. 41404061).

References

- An, M., Wiens, D.A., Zhao, Y., Feng, M., Nyblade, A.A., Kanao, M., Li, Y., Maggi, A., Lévéque, J.J., 2015. S-velocity model and inferred Moho topography beneath the Antarctic Plate from Rayleigh waves. *J. Geophys. Res. B: Solid Earth* 120:359–383. <http://dx.doi.org/10.1002/2014JB011332>.
- Audet, P., Bürgmann, R., 2011. Dominant role of tectonic inheritance in supercontinent cycles. *Nat. Geosci.* 4:184–187. <http://dx.doi.org/10.1038/ngeo1080>.
- Audet, P., Mareschal, J.C., 2007. Wavelet analysis of the coherence between Bouguer gravity and topography: application to the elastic thickness anisotropy in the Canadian Shield. *Geophys. J. Int.* 168:287–298. <http://dx.doi.org/10.1111/j.1365-246X.2006.03231.x>.
- Banks, R.J., Parker, R.L., Huestis, S.P., 1977. Isostatic compensation on a continental scale: local versus regional mechanisms. *Geophys. J. R. Astron. Soc.* 51, 431–452.
- Behrendt, J.C., 1999. Crustal and lithospheric structure of the west Antarctic Rift System from geophysical investigations – a review. *Glob. Planet. Chang.* 23:25–44. [http://dx.doi.org/10.1016/S0921-8181\(99\)00049-1](http://dx.doi.org/10.1016/S0921-8181(99)00049-1).
- Boger, S.D., 2011. Antarctica – before and after Gondwana. *Gondwana Res.* 19:335–371. <http://dx.doi.org/10.1016/j.gr.2010.09.003>.
- Burov, E.B., Diamant, M., 1995. The effective elastic thickness (T_e) of continental lithosphere: what does it really mean? *J. Geophys. Res.* 100:3905. <http://dx.doi.org/10.1029/94JB02770>.
- Chen, B., Kaban, M.K., El Khrepy, S., Al-Arifi, N., 2015a. Effective elastic thickness of the Arabian plate: weak shield versus strong platform. *Geophys. Res. Lett.* 42: 3298–3304. <http://dx.doi.org/10.1002/2015GL063725>.
- Chen, B., Liu, J., Chen, C., Du, J., Sun, Y., 2015b. Elastic thickness of the Himalayan–Tibetan orogen estimated from the fan wavelet coherence method, and its implications for lithospheric structure. *Earth Planet. Sci. Lett.* 409:1–14. <http://dx.doi.org/10.1016/j.epsl.2014.10.039>.
- Close, D.I., Stagg, H.M.J., O'Brien, P.E., 2007. Seismic stratigraphy and sediment distribution on the Wilkes Land and Terre Adélie margins, East Antarctica. *Mar. Geol.* 239:33–57. <http://dx.doi.org/10.1016/j.margeo.2006.12.010>.
- Dalziel, I.W.D., Elliot, D.H., 1982. West Antarctica: problem child of Gondwanaland. *Tectonics* 1:3–19. <http://dx.doi.org/10.1029/TC001i001p00003>.
- Dorman, L.M., Lewis, B.T.R., 1970. Experimental isostasy: 1. Theory of the determination of the Earth's isostatic response to a concentrated load. *J. Geophys. Res.* 75:3357. <http://dx.doi.org/10.1029/JB075i017p03357>.

- Fanning, C.M., Flint, R.B., Parker, A.J., Ludwig, K.R., Blissett, A.H., 1988. Refined Proterozoic evolution of the Gawler Craton, South Australia, through U-Pb zircon geochronology. *Precambrian Res.* 40–41:363–386. [http://dx.doi.org/10.1016/0301-9268\(88\)90076-9](http://dx.doi.org/10.1016/0301-9268(88)90076-9).
- Ferraccioli, F., Finn, C.A., Jordan, T., Bell, R.E., Anderson, L., Damaske, S., 2011. East Antarctic rifting triggers uplift of the Gamburtsev Mountains. *Nature* 479:388–392. <http://dx.doi.org/10.1038/nature10566>.
- Fisher, A.T., Mankoff, K.D., Tulaczyk, S.M., Tyler, S.W., 2015. High Geothermal Heat Flux Measured Below the West Antarctic Ice Sheet 1–9.
- Föltmann, T., Oliver, R., 1994. Review of Precambrian-Palaeozoic relationships at the craton margins of southeastern Australia and adjacent Antarctica. *Precambrian Res.* 69: 293–306. [http://dx.doi.org/10.1016/0301-9268\(94\)90093-0](http://dx.doi.org/10.1016/0301-9268(94)90093-0).
- Förste, C., Bruinsma, S.L., Abrilovskov, O., Lemoinne, J.-M., Marty, J.C., Flechner, F., Balmino, G., Barthelmes, F., Biancale, R., 2014. EIGEN-6C4 the latest combined global gravity field model including GOCE data up to degree and order 2190 of GFZ Potsdam and GRGS Toulouse. *GFZ Data Services* <http://dx.doi.org/10.5880/icgem.2015.1>.
- Forsyth, D.W., 1985. Subsurface loading and estimates of the flexural rigidity of continental lithosphere. *J. Geophys. Res. Planets* 90:12623–12632. <http://dx.doi.org/10.1029/JB090iB14p12623>.
- Fretwell, P., Pritchard, H.D., Vaughan, D.G., Bamber, J.L., Barrand, N.E., Bell, R., Bianchi, C., Bingham, R.G., Blankenship, D.D., Casassa, G., Catania, G., Callens, D., Conway, H., Cook, A.J., Corr, H.F.J., Damaske, D., Damm, V., Ferraccioli, F., Forsberg, R., Fujita, S., Gim, Y., Gogineni, P., Griggs, J.A., Hindmarsh, R.C.A., Holmlund, P., Holt, J.W., Jacobel, R.W., Jenkins, A., Jokat, W., Jordan, T., King, E.C., Kohler, J., Krabill, W., Riger-Kusk, M., Langley, K.A., Leitchenkov, G., Leuschen, C., Luyendyk, B.P., Matsuoka, K., Mouginot, J., Nitsche, F.O., Nogi, Y., Nost, O.A., Popov, S.V., Rignot, E., Rippin, D.M., Rivera, A., Roberts, J., Ross, N., Siegert, M.J., Smith, A.M., Steinhage, D., Studinger, M., Sun, B., Tinto, B.K., Welch, B.C., Wilson, D., Young, D.A., Xiangbin, C., Zirizzotti, A., 2013. Bedmap2: improved ice bed, surface and thickness datasets for Antarctica. *Cryosphere* 7:373–393. <http://dx.doi.org/10.5194/tc-7-373-2013>.
- Goes, S., Govers, R., Vacher, P., 2000. Shallow mantle temperatures under Europe from P and S wave tomography. *J. Geophys. Res.* 105:11153. <http://dx.doi.org/10.1029/1999JB900300>.
- Harrowfield, M., Holdgate, G.R., Wilson, C.J.L., McLoughlin, S., 2005. Tectonic significance of the Lambert graben, East Antarctica: reconstructing the Gondwanan rift. *Geology* 33:197–200. <http://dx.doi.org/10.1130/G21081.1>.
- Hole, M.J., LeMasurier, W.E., 1994. Tectonic controls on the geochemical composition of Cenozoic, mafic alkaline volcanic rocks from West Antarctica. *Contrib. Mineral. Petrol.* 117:187–202. <http://dx.doi.org/10.1007/BF00286842>.
- Huerta, A.D., Harry, D.L., 2007. The transition from diffuse to focused extension: modeled evolution of the West Antarctic Rift system. *Earth Planet. Sci. Lett.* 255:133–147. <http://dx.doi.org/10.1016/j.epsl.2006.12.011>.
- Kaban, M.K., El Khrepy, S., Al-Arif, N., 2016. Isostatic model and isostatic gravity anomalies of the Arabian Plate and surroundings. *Pure Appl. Geophys.* 173:1211–1221. <http://dx.doi.org/10.1007/s00024-015-1164-0>.
- Kirby, J.F., 2005. Which wavelet best reproduces the Fourier power spectrum? *Comput. Geosci.-UK* 31 (7):846–864. <http://dx.doi.org/10.1016/j.cageo.2005.01.014>.
- Kirby, J.F., 2014. Estimation of the effective elastic thickness of the lithosphere using inverse spectral methods: the state of the art. *Tectonophysics* <http://dx.doi.org/10.1016/j.tecto.2014.04.021>.
- Kirby, J.F., Swain, C.J., 2004. Global and local isostatic coherence from the wavelet transform. *Geophys. Res. Lett.* 31:1–5. <http://dx.doi.org/10.1029/2004GL021569>.
- Kirby, J.F., Swain, C.J., 2006. Mapping the mechanical anisotropy of the lithosphere using a 2D wavelet coherence, and its application to Australia. *Phys. Earth Planet. Inter.* 158: 122–138. <http://dx.doi.org/10.1016/j.pepi.2006.03.022>.
- Kirby, J.F., Swain, C.J., 2008. An accuracy assessment of the fan wavelet coherence method for elastic thickness estimation. *Geochem. Geophys. Geosyst.* 9. <http://dx.doi.org/10.1029/2007GC001773>.
- Kirby, J.F., Swain, C.J., 2009. A reassessment of spectral T_e estimation in continental interiors: the case of North America. *J. Geophys. Res. Solid Earth* 114:1–36. <http://dx.doi.org/10.1029/2009JB006356>.
- Kirby, J.F., Swain, C.J., 2011. Improving the spatial resolution of effective elastic thickness estimation with the fan wavelet transform. *Comput. Geosci.* 37:1345–1354. <http://dx.doi.org/10.1016/j.cageo.2010.10.008>.
- Laske, G., Masters, G., 2013. Update on CRUST1.0—A 1-degree global model of Earth's crust. *EGU Gen. Assem.* 15, 2658.
- Lisker, F., Brown, R., Fabel, D., 2003. Denudational and thermal history along a transect across the Lambert graben, northern Prince Charles Mountains, Antarctica, derived from apatite fission track thermochronology. *Tectonics* 22:1055. <http://dx.doi.org/10.1029/2002TC001477>.
- Lowry, A.R., Smith, R.B., 1994. Flexural rigidity of the Basin and Range–Colorado Plateau–Rocky Mountain transition from coherence analysis of gravity and topography. *J. Geophys. Res. Solid Earth* 99 (B10), 20123–20140.
- Lythe, M.B., Vaughan, D.G., BEDMAP Consortium, 2001. BEDMAP: a new ice thickness and subglacial topographic model of Antarctica. *J. Geophys. Res. Solid Earth* 106: 11335–11351. <http://dx.doi.org/10.1029/2000JB000449>.
- Maule, C.F., Purucker, M.E., Olsen, N., Mosegaard, K., 2005. Heat flux anomalies in Antarctica revealed by satellite magnetic data. *Science* 309:464–467 (80). <http://dx.doi.org/10.1126/science.1106888>.
- McKenzie, D., 2003. Estimating Te in the presence of internal loads. *J. Geophys. Res.* 108 (B9):2438. <http://dx.doi.org/10.1029/2002JB001766>.
- McKenzie, D., Bowin, C., 1976. The relationship between bathymetry and gravity in the Atlantic Ocean. *J. Geophys. Res.* 81, 1903–1915.
- McKenzie, D., Fairhead, D., 1997. Estimates of the effective elastic thickness of the continental lithosphere from Bouguer and free air gravity anomalies. *J. Geophys. Res. Solid Earth* 102 (B12), 27523–27552.
- McKenzie, D., Yi, W., Rummel, R., 2015. Estimates of Te for continental regions using GOCE gravity. *Earth Planet. Sci. Lett.* 428:97–107. <http://dx.doi.org/10.1016/j.epsl.2015.07.036>.
- Morelli, A., Danesi, S., 2004. Seismological imaging of the Antarctic continental lithosphere: a review. *Glob. Planet. Chang.*:155–165 <http://dx.doi.org/10.1016/j.gloplacha.2003.12.005>.
- Mukasa, S.B., Dalziel, I.W.D., 2000. Marie Byrd Land, West Antarctica: evolution of Gondwana's Pacific margin constrained by zircon U-Pb geochronology and feldspar common- Pb isotopic compositions. *Geol. Soc. Am. Bull.* 112:611–627. [http://dx.doi.org/10.1130/0016-7606\(2000\)112<0611:MBLWAE>2.3.CO;2](http://dx.doi.org/10.1130/0016-7606(2000)112<0611:MBLWAE>2.3.CO;2).
- O'Donnell, J.P., Nyblade, A.A., 2014. Antarctica's hypsometry and crustal thickness: implications for the origin of anomalous topography in East Antarctica. *Earth Planet. Sci. Lett.* 388:143–155. <http://dx.doi.org/10.1016/j.epsl.2013.11.051>.
- Paxman, G.J.G., Watts, A.B., Ferraccioli, F., Jordan, T.A., Bell, R.E., Jamieson, S.S.R., Finn, C.A., 2016. Erosion-driven uplift in the Gamburtsev Subglacial Mountains of East Antarctica. *Earth Planet. Sci. Lett.* 452:1–14. <http://dx.doi.org/10.1016/j.epsl.2016.07.040>.
- Pérez-Gussinyé, M., Watts, A.B., 2005. The long-term strength of Europe and its implications for plate-forming processes. *Nature* 436:381–384. <http://dx.doi.org/10.1038/nature03854>.
- Pérez-Gussinyé, M., Lowry, A.R., Watts, A.B., Velicogna, I., 2004. On the recovery of effective elastic thickness using spectral methods: examples from synthetic data and from the Fennoscandian Shield. *J. Geophys. Res.* 109:B10409. <http://dx.doi.org/10.1029/2003JB002788>.
- Pérez-Gussinyé, M., Metois, M., Fernández, M., Vergés, J., Fullea, J., Lowry, A.R., 2009. Effective elastic thickness of Africa and its relationship to other proxies for lithospheric structure and surface tectonics. *Earth Planet. Sci. Lett.* 287, 152–167.
- Petrunin, A.G., Rogozhina, I., Vaughan, A.P.M., Kukkonen, I.T., Kaban, M.K., Koulakov, I., Thomas, M., 2013. Heat flux variations beneath central Greenland's ice due to anomalously thin lithosphere. *Nat. Geosci.* 6:746–750. <http://dx.doi.org/10.1038/geo1898>.
- Phillips, G., Lüüfer, A.L., 2009. Brittle deformation relating to the Carboniferous-Cretaceous evolution of the Lambert Graben, East Antarctica: a precursor for Cenozoic relief development in an intraplate and glaciated region. *Tectonophysics* 471:216–224. <http://dx.doi.org/10.1016/j.tecto.2009.02.012>.
- Powell, C.M., Roots, S.R., Veevers, J.J., 1988. Pre-breakup continental extension in East Gondwanaland and the early opening of the eastern Indian Ocean. *Tectonophysics* 155:261–283. [http://dx.doi.org/10.1016/0040-1951\(88\)90269-7](http://dx.doi.org/10.1016/0040-1951(88)90269-7).
- Price, P.B., Nagornov, O.V., Bay, R., Chirkin, D., He, Y., Miocinovic, P., Richards, A., Woschnagg, K., Koci, B., Zagorodnov, V., 2002. Temperature profile for glacial ice at the South Pole: implications for life in a nearby subglacial lake. *Proc. Natl. Acad. Sci. U. S. A.* 99:7844–7847. <http://dx.doi.org/10.1073/pnas.082238999>.
- Ramillien, G., Lombard, A., Cazenave, A., Ivens, E.R., Llubes, M., Biancale, R., 2006. Interannual variations of the mass balance of the Antarctica and Greenland ice sheets from GRACE. *Glob. Planet. Chang.* 53:198–208. <http://dx.doi.org/10.1016/j.gloplacha.2006.06.003>.
- Reading, A.M., 2006. The seismic structure of Precambrian and early Palaeozoic terranes in the Lambert Glacier region, East Antarctica. *Earth Planet. Sci. Lett.* 244:44–57. <http://dx.doi.org/10.1016/j.epsl.2006.01.031>.
- Reading, A.M., 2007. The seismicity of the Antarctic plate. *Geol. Soc. Am. Spec. Pap.* 425: 285–298. [http://dx.doi.org/10.1130/2007.2425\(18\)](http://dx.doi.org/10.1130/2007.2425(18)).
- Rignot, E., Mouginot, J., Scheuchl, B., 2011. Ice flow of the Antarctic Ice Sheet. *Science* 333: 1427–1430 (80). <http://dx.doi.org/10.1126/science.1208336>.
- Schaeffer, A.J., Lebedev, S., 2013. Global shear speed structure of the upper mantle and transition zone. *Geophys. J. Int.* 194:417–449. <http://dx.doi.org/10.1093/gji/ggt095>.
- Schaffer, J., Timmermann, R., Arndt, J.E., Steinhage, D., Kanzow, T., 2014. RTopo-2: a global dataset of ice sheet topography, cavity geometry and ocean bathymetry to study ice-ocean interaction in Northeast Greenland. *REKLIM Conf. "Our Clim. - Our Future."* Berlin, Ger. 6 Oct. 2014–9 Oct. 2014.
- Scheinert, M., Ferraccioli, F., Schwabe, J., Bell, R., Studinger, M., Damaske, D., Jokat, W., Alešhková, N., Jordan, T., Leitchenkov, G., Blankenship, D.D., Damiani, T.M., Young, D., Cochran, J.R., Richter, T.D., 2016. New Antarctic gravity anomaly grid for enhanced geodetic and geophysical studies in Antarctica. *Geophys. Res. Lett.* 43:600–610. <http://dx.doi.org/10.1002/2015GL067439>.
- Shapiro, N.M., Ritzwoller, M.H., 2004. Inferring surface heat flux distributions guided by a global seismic model: particular application to Antarctica. *Earth Planet. Sci. Lett.* 223: 213–224. <http://dx.doi.org/10.1016/j.epsl.2004.04.011>.
- Simons, F.J., Zuber, M.T., Korenaga, J., 2000. Isostatic response of the Australian lithosphere: estimation of effective elastic thickness and anisotropy using multitaper spectral analysis. *J. Geophys. Res.* 105:19163–19184. <http://dx.doi.org/10.1029/2000JB000157>.
- Sleep, N.H., 2006. Mantle plumes from top to bottom. *Earth-Science Rev.* 77:231–271. <http://dx.doi.org/10.1016/j.earscirev.2006.03.007>.
- Smith, A.G., Drewry, D.J., 1984. Delayed phase change due to hot asthenosphere causes Transantarctic uplift? *Nature* 309, 536–538.
- Snyder, J.P., 1987. Map Projections – A Working Manual. U.S. Geological Survey Professional Paper. US Government Printing Office.
- Stark, C.P., Stewart, J., Ebinger, C.J., 2003. Wavelet transform mapping of effective elastic thickness and plate loading: validation using synthetic data and application to the study of southern African tectonics. *J. Geophys. Res.* 108 (B12):2558. <http://dx.doi.org/10.1029/2001JB000609>.
- Stern, T.A., ten Brink, U.S., 1989. Flexural uplift of the Transantarctic Mountains. *J. Geophys. Res. Solid Earth* 94:10315–10330. <http://dx.doi.org/10.1029/JB094iB08p10315>.
- ten Brink, U., Stern, T., 1992. Rift flank uplifts and hinterland basins – comparison of the Transantarctic Mountains with the great escarpment of Southern Africa. *J. Geophys. Res. Earth* 97:569–585. <http://dx.doi.org/10.1029/91JB02231>.

- ten Brink, U.S., Hackney, R.I., Bannister, S., Stern, T.A., 1997. **Uplift of the Transantarctic Mountains and the bedrock.** *J. Geophys. Res.* 102, 27603–27621.
- Tesauro, M., Audet, P., Kaban, M.K., Brägmann, R., Cloetingh, S., 2012. The effective elastic thickness of the continental lithosphere: comparison between rheological and inverse approaches. *Geochem. Geophys. Geosyst.* 13:1–18. <http://dx.doi.org/10.1029/2012GC004162>.
- Tesauro, M., Kaban, M.K., Mooney, W.D., 2015. Variations of the lithospheric strength and elastic thickness in North America. *Geochem. Geophys. Geosyst.* 16:2197–2220. <http://dx.doi.org/10.1002/2015GC005937>.
- Thompson, D.J., 1982. **Spectrum estimation and harmonic analysis.** *Proc. IEEE* 70, 1055–1096.
- Thomson, S.N., Reiners, P.W., Hemming, S.R., Gehrels, G.E., 2013. The contribution of glacial erosion to shaping the hidden landscape of East Antarctica. *Nat. Geosci.* 6: 203–207. <http://dx.doi.org/10.1038/ngeo1722>.
- Torsvik, T.H., Steinberger, B., Gurnis, M., Gaina, C., 2010. Plate tectonics and net lithosphere rotation over the past 150 my. *Earth Planet. Sci. Lett.* 291:106–112. <http://dx.doi.org/10.1016/j.epsl.2009.12.055>.
- van Wijk, J.W., Lawrence, J.F., Driscoll, N.W., 2008. Formation of the Transantarctic Mountains related to extension of the West Antarctic Rift system. *Tectonophysics* 458: 117–126. <http://dx.doi.org/10.1016/j.tecto.2008.03.009>.
- Veevers, J.J., 2007. Pan-Gondwanaland post-collisional extension marked by 650–500 Ma alkaline rocks and carbonatites and related detrital zircons: a review. *Earth-Science Rev.* 83:1–47. <http://dx.doi.org/10.1016/j.earscirev.2007.03.001>.
- Veevers, J.J., 2012. Reconstructions before rifting and drifting reveal the geological connections between Antarctica and its conjugates in Gondwanaland. *Earth-Sci. Rev.* 111:249–318. <http://dx.doi.org/10.1016/j.earscirev.2011.11.009>.
- Watts, A.B., 1978. **An analysis of isostasy in the world's oceans, 1, Hawaiian-Emperor seamount chain.** *J. Geophys. Res.* 83, 5989–6004.
- Watts, A.B., 2001. **Isostasy and Flexure of the Lithosphere.** Cambridge University Press.
- Watts, A.B., Sandwell, D.T., Smith, W.H.F., Wessel, P., 2006. **Global gravity, bathymetry, and the distribution of submarine volcanism through space and time.** *J. Geophys. Res. Solid Earth* 111 (B8).
- Willett, S.D., Chapman, D.S., Neugebauer, H.J., 1985. A thermo-mechanical model of continental lithosphere. *Nature* 314:520–523. <http://dx.doi.org/10.1038/314520a0>.
- Yamasaki, T., Miura, H., Nogi, Y., 2008. Numerical modelling study on the flexural uplift of the Transantarctic Mountains. *Geophys. J. Int.* 174:377–390. <http://dx.doi.org/10.1111/j.1365-246X.2008.03815.x>.